

# A numerical study of the impurity effects of nitrogen and sulfur dioxide on the solubility trapping of carbon dioxide geological storage

Didi Li <sup>a</sup>, Xi Jiang <sup>a,b,\*</sup>

<sup>a</sup>Department of Safety Science Engineering & State Key Laboratory of Fire Science, University of Science and Technology of China, Hefei, Anhui 230026, China

<sup>b</sup>Engineering Department, Lancaster University, Lancaster LA1 4YR, UK

## HIGHLIGHTS

- Effects of N<sub>2</sub> and SO<sub>2</sub> impurity on CO<sub>2</sub> solubility trapping are investigated.
- Higher N<sub>2</sub> impurity leads to later onset of convection and smaller dissolution rate.
- With N<sub>2</sub> impurity the total CO<sub>2</sub> dissolved is less than that of injecting CO<sub>2</sub> alone.
- SO<sub>2</sub> impurity is implied to enhance the solubility trapping mechanism.
- SO<sub>2</sub> impurity effect is more significant than N<sub>2</sub> at the same impurity concentration.

## ARTICLE INFO

### Article history:

Received 21 February 2014

Received in revised form 2 April 2014

Accepted 16 April 2014

Available online 8 May 2014

### Keywords:

Carbon capture and storage

Impurity

Solubility trapping

Numerical simulation

## ABSTRACT

Three-dimensional numerical simulations are performed to investigate the effects of nitrogen (N<sub>2</sub>) and sulfur dioxide (SO<sub>2</sub>) impurities on the solubility trapping mechanism of carbon dioxide (CO<sub>2</sub>) geological storage. Dissolved CO<sub>2</sub> has been suggested to increase the density of the aqueous phase. Results from this study indicate that, when dissolved in the formation water, certain level of the N<sub>2</sub> impurity contained in the CO<sub>2</sub> streams reduces the density increase, which is the driving force of convection. With a higher N<sub>2</sub> concentration, the onset of convection is later and the dissolution rate is smaller. The decay time of convection for the higher N<sub>2</sub> concentration case is also delayed. For the co-injection of CO<sub>2</sub> and N<sub>2</sub>, total CO<sub>2</sub> dissolved in the formation fluids is less than that of injecting CO<sub>2</sub> alone. During the timescale of dissolution, the mobile and buoyant CO<sub>2</sub> streams have the potential to leak through the caprock to the atmosphere. It is necessary to reinforce the risk management for safe CO<sub>2</sub> storage for the co-injection of CO<sub>2</sub> and N<sub>2</sub>. In contrary to N<sub>2</sub>, the SO<sub>2</sub> impurity is implied to enhance the solubility trapping mechanism and it has more significant effects compared to N<sub>2</sub> at the same impurity concentration.

© 2014 Elsevier Ltd. All rights reserved.

## 1. Introduction

Carbon capture and storage (CCS) is a promising option to reduce greenhouse gas emissions into the atmosphere [1,2]. The CO<sub>2</sub> streams captured generally contain a variety of impurities, such as N<sub>2</sub>, SO<sub>x</sub>, O<sub>2</sub>, Ar and H<sub>2</sub>O [3,4]. It is estimated that the costs of CO<sub>2</sub> capture, including separation and compression, account for about 75% of the total CCS costs [5,6]. Impure CO<sub>2</sub> capture and storage has currently been operated or planned to cut down the capture costs and thus the overall costs of CCS. However, the existence of impurities, for instance, N<sub>2</sub>, SO<sub>x</sub>, and Ar, in the CO<sub>2</sub>

streams may lead to an increase in both the transportation and storage costs. It is necessary to investigate and evaluate the effects of each impurity on the capture, transportation and storage processes to realize optimum benefits and establish the regulatory framework for CCS. Nicot et al. [7] pointed out that the impact of impurities was more marked at shallow depths. N<sub>2</sub> is the largest constituent of air and data from the COORAL study [8] suggested that N<sub>2</sub> was the main impurity of the CO<sub>2</sub> streams no matter which carbon capture technology [9] was employed. Experimental and numerical methods have been adopted to study the effects of N<sub>2</sub> impurity on the transportation part [10–12]. The results implied that N<sub>2</sub> concentration should be limited for the design and operation of the pipeline transport. However, there is a lack of in-depth investigations focusing on the effects of N<sub>2</sub> on the trapping mechanisms with respect to the short-term and/or long-term geological storage.

\* Corresponding author at: Engineering Department, Lancaster University, Lancaster LA1 4YR, UK. Tel.: +44 1524 592439; fax: +44 1524 381707.

E-mail address: x.jiang@lancaster.ac.uk (X. Jiang).

## Nomenclature

$b$	mole fraction of gas phase in the system	$X, Y, Z$	Cartesian coordinates
$c_0$	constant for the onset time	$Y$	component mole fraction in gas phase
$D$	gas diffusivity in aqueous phase ( $\text{m}^2/\text{s}$ )	$z$	component mole fraction in the feed system, assumed to be known
$D_{mn}$	distance between mesh $m$ and $n$ (m)		
$f$	scaling factor		
$G$	mesh volume ( $\text{m}^3$ )		
$g$	magnitude of gravitational acceleration ( $\text{m}/\text{s}^2$ )		
$\mathbf{g}$	vector of gravitational acceleration ( $\text{m}/\text{s}^2$ )		
$H$	height of the simulation domain (m)		
$K$	permeability ( $\text{m}^2$ )		
$\mathbf{K}$	permeability tensor ( $\text{m}^2$ )		
$K_i$	equilibrium constant		
$k$	relative permeability		
$M$	molecular weight		
$\mathbf{n}$	normal vector on the mesh volume, pointing inwards		
$P$	pressure (Pa)		
$Ra$	Rayleigh number		
$r$	source/sink term ( $\text{mol}/\text{m}^3/\text{s}$ )		
$rn$	random number in the range 0–1		
$S$	phase saturation		
$t$	time (s)		
$T$	temperature (K)		
$V$	partial molar volume of dissolved gas ( $\text{m}^3/\text{mol}$ )		
$\mathbf{v}$	Darcy velocity ( $\text{m}/\text{s}$ )		
$x$	component mole fraction in aqueous phase		
			<i>Greek symbols</i>
			$\Gamma$ surface area of connected mesh interface ( $\text{m}^2$ )
			$\alpha, \beta$ fluid phase
			$\gamma$ intersection angle between $\mathbf{g}$ and the line from mesh $n$ to $m$
			$\phi$ porosity
			$\rho$ density ( $\text{kg}/\text{m}^3$ )
			$\sum$ summation
			$\mu$ dynamic viscosity (Pa s)
			<i>Subscripts/superscripts</i>
			$c$ capillary
			$i$ component index
			$m, n$ grid block index
			$mn$ averaging between mesh $m$ and $n$ , including harmonic and upstream weightings
			$o$ molar unit
			$onset$ onset time of convection
			$r$ relative permeability
			$w$ water

As listed in Table 1,  $\text{SO}_2$  usually does not account for as high as a percentage compared with  $\text{N}_2$  [13]. However, this impurity is rather hazardous itself. The emissions of  $\text{SO}_2$  should be controlled for the environmental and human health considerations. The disposal of  $\text{SO}_2$  along with  $\text{CO}_2$  in the CCS projects seems an economical and feasible way [14]. The corrosion effects of  $\text{SO}_2$  on the pipeline transport have been investigated by some studies [15–17]. Numerical simulations have been carried out to study the reactivity of  $\text{SO}_2$  in the subsurface and rather contradictory conclusions have been drawn [5,18–20]. Some investigations suggested that co-injection of  $\text{CO}_2$  and  $\text{SO}_2$  could cause enhanced brine acidification and significantly change the formation porosity [5,18]. Results of some simulations implied that the inclusion of  $\text{SO}_2$  did not cause rapid, significant porosity change, especially when the amount of  $\text{SO}_2$  was small [19,20]. Most of the simulations have either assumed that  $\text{SO}_2$  was injected as an aqueous solution or the water in the injection zone was never dry, which would be relevant for injection of  $\text{CO}_2$  with water. The important point is that  $\text{SO}_2$  is far less reactive when it is dry. Therefore, the brine acidification and porosity change in these simulations may have been exaggerated. Furthermore, geochemical reactions generally occur on relatively longer timescales [2], usually more than 1000 years, which is far beyond the time scale of many investigations. More importantly, most of the simulations did not model the mineral buffering reactions. Ellis et al. [21] predicted that as mineral dissolution and resultant pH buffering was likely to occur during the timeframe of acidification, especially for the formations with sufficient carbonate basic silicate or basic aluminosilicate minerals, the potential for brine acidification would be further reduced. Apart

from the complexity and uncertainty of the reactivity and brine acidification effects of  $\text{SO}_2$ , the influence of the physical property of this impurity should be brought to the forefront to obtain a better understanding of the co-injection and storage of  $\text{CO}_2$  with  $\text{SO}_2$ .

For  $\text{CO}_2$  geological storage, there are three main potential storage options: depleted oil and gas reservoirs, deep saline formations and unminable coal beds [1,2]. All the potential storage sites contain aqueous phases [5]. This study focuses primarily on the deep saline formations because of their large potential storage capacity and proximity to point sources [1–3]. The injected gas mixtures will dissolve into the formation fluids and this mechanism is called as “solubility trapping” [22,23]. Generally, the  $\text{CO}_2$  streams are injected at depths below 800 m, where the  $\text{CO}_2$  streams exist in a relatively dense supercritical state [1] (the “supercritical” is occasionally referred to as “gas” for simplicity below). The density of the  $\text{CO}_2$  streams is still lower than that of the formation fluids in situ. Due to the buoyancy force, the  $\text{CO}_2$  streams flow upwards, accumulate and spread horizontally under the low-permeability barriers, such as shales and/or caprocks [2]. If there are any high-permeability regions and/or anthropogenic pathways in the low-permeability barriers like fractures and abandoned wells, the buoyant and mobile  $\text{CO}_2$  streams may leak from the storage sites [2,22]. Along with molecular diffusion, the supercritical fluids slowly dissolve into the formation fluids. The dissolution of  $\text{CO}_2$  has been demonstrated to result in a local density increase of the aqueous phase at the two phase interface, leading to a convective instability [24–26]. The convective mixing results in a much higher dissolution rate than pure diffusion. Dissolved  $\text{CO}_2$  is considered trapped, because the  $\text{CO}_2$ -rich aqueous fluids, in the form of  $\text{CO}_2$ -concentrated fingers, move very slowly and will most likely migrate downwards [27]. The dissolved  $\text{CO}_2$  also has the potential to react with the rock minerals to form carbonate minerals over long time scales.

Although the process of the convective mixing has been investigated extensively, only a few studies took the three-dimensional (3D) effects into consideration. Numerical simulations employing

**Table 1**

The range of compositions of  $\text{N}_2$  and  $\text{SO}_2$  in the captured  $\text{CO}_2$  streams.

Component	Min mol%	Max mol%
$\text{N}_2$	0.02	10
$\text{SO}_2$	<0.0001	1.5

two grid resolutions have been performed to investigate the impact of the Rayleigh instability (convective instability) on the long-term CO<sub>2</sub> geological storage. However, convergence was not obtained even for the finer grid spacing [28]. By adopting a block-structured adaptive mesh refinement method, Pau et al. [29] carried out 3D simulations and suggested that the simplification to a two-dimensional model did have an impact on the accuracy of the predictions of the solubility trapping mechanism. More importantly, most of the previous studies did not account for the effects of impurities. It was indicated that the dissolution of H<sub>2</sub>S decreased the density of the dissolved aqueous phase and the co-injection of H<sub>2</sub>S with CO<sub>2</sub> was negative to the solubility trapping mechanism [6]. However, that study did not investigate the short-term or long-term behaviors of the convective mixing process. The goal of this study is to investigate and analyze the effects of N<sub>2</sub> and SO<sub>2</sub> impurities on the solubility trapping mechanism by carrying out 3D numerical simulations.

## 2. Physical model

### 2.1. Model setup

In the present study, the injection depth is about 1000 m in the subsurface. As shown in Fig. 1a, there is an interface separating the injected CO<sub>2</sub> streams above from the formation aqueous phase below. A 3D domain below the interface is selected as the research domain. The size of the chosen cube is 1 m × 1 m × 1 m. The interface is assumed to be horizontal during the simulations. The ambient aqueous phase is supposed to be pure water. The typical simulation parameters, including the fluid properties and formation parameters, at the chosen depth are listed in Table 2. Table 3 lists the critical points of CO<sub>2</sub>, N<sub>2</sub> and SO<sub>2</sub>. It can be seen that both the critical temperature and pressure of N<sub>2</sub> are lower than that of CO<sub>2</sub>. Thus, CO<sub>2</sub> and N<sub>2</sub> mixture exists as supercritical fluids under the specified conditions. CO<sub>2</sub> and SO<sub>2</sub> share similar critical

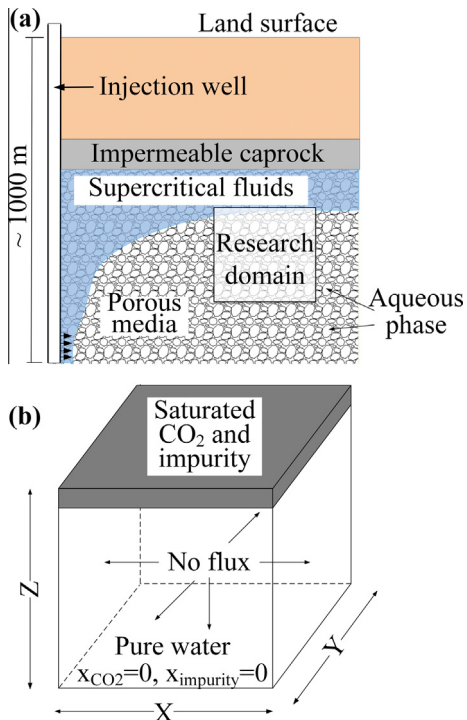


**Fig. 1.** Schematic of the model domain for the solubility trapping mechanism, (a) domain representation and (b) mathematical model.

**Table 2**  
Fluid properties and formation parameters.

Pressure (Pa)	$1 \times 10^7$
Temperature (K)	318.15
Pure water density (kg/m <sup>3</sup> )	994.56
Pure water viscosity (Pa s)	$0.5947 \times 10^{-3}$
CO <sub>2</sub> diffusivity (m <sup>2</sup> /s)	$2 \times 10^{-9}$
N <sub>2</sub> diffusivity (m <sup>2</sup> /s)	$2 \times 10^{-9}$
SO <sub>2</sub> diffusivity (m <sup>2</sup> /s)	$2 \times 10^{-9}$
Gravitational acceleration (m/s <sup>2</sup> )	9.81
Permeability (m <sup>2</sup> )	$1.0 \times 10^{-11}$
Salinity	0
Porosity	0.3

pressures while the critical temperature of SO<sub>2</sub> is much higher than the chosen ambient temperature. According to Crandell et al. [14], small amounts of SO<sub>2</sub> would not have a noticeable effect on the critical point of the CO<sub>2</sub> streams. For the SO<sub>2</sub> concentrations chosen for our simulations, the CO<sub>2</sub> and SO<sub>2</sub> streams can be treated as supercritical fluids. Geochemical reactions generally occur on long timescales [2] while the length of our simulation time is less than one year which is much shorter. Consequently, geochemical reactions are not taken into account. In addition, for the dissolution of gases into the formation water, thermal effects are neglected, i.e., isothermal conditions are employed in the model.

### 2.2. Governing equations

The governing equations of the flow and transport processes of the fluids and heat in porous media are derived from conservation laws. The heat transfer is not considered in this study and thus the energy conservation equation is not set up. The momentum conservation equation commonly used for multiphase fluid flow in porous media is the generalized form of Darcy's law [30], which can be derived from the Navier-Stokes momentum equations. The general integral form of the governing equations can be written as follows:

$$\begin{aligned} \frac{\partial}{\partial t} \int_G \phi \sum_{\alpha} S_{\alpha} \rho_{o,\alpha} x_{\alpha}^i dG - \int_{\Gamma} \left( \sum_{\alpha} \rho_{o,\alpha} \mathbf{v}_{\alpha} x_{\alpha}^i \right) \cdot \mathbf{n} d\Gamma \\ + \int_{\Gamma} \left( \phi \sum_{\alpha} S_{\alpha} D_{\alpha} \rho_{o,\alpha} \nabla x_{\alpha}^i \right) \cdot \mathbf{n} d\Gamma \\ = \int_G r^i dG \end{aligned} \quad (1)$$

$$\mathbf{v}_{\alpha} = -K \frac{k_{r\alpha}}{\mu_{\alpha}} (\nabla P_{\alpha} - \rho_{\alpha} \mathbf{g}) \quad (2)$$

with the supplementary constraints:

$$\sum_{\alpha} S_{\alpha} = 1 \quad (3)$$

and

$$P_{\alpha} = P_{\beta} - P_{c,\beta\alpha}; \quad \forall \alpha, \beta, \alpha \neq \beta \quad (4)$$

The mass conservation equations consist of four parts representing all the possible mass transfer mechanisms, i.e., the time derivative, convective flux, diffusive flux and the source/sink

**Table 3**  
Critical points of CO<sub>2</sub>, N<sub>2</sub> and SO<sub>2</sub>.

Component	Critical temperature (K)	Critical pressure (Pa)
CO <sub>2</sub>	304.19	$7.38 \times 10^6$
N <sub>2</sub>	126.19	$3.40 \times 10^6$
SO <sub>2</sub>	430.64	$7.88 \times 10^6$

respectively. The governing equations of multiphase fluids demonstrate rather strong nonlinearity because of the nonlinear dependence of the saturation on both the relative permeability  $k_{r\alpha}$  and the capillary pressure  $P_{c,\beta\alpha}$ . Instead of dealing with complicated two fluid phases, the gas layer overlying the aqueous phase is modeled as a boundary condition of formation water saturated with CO<sub>2</sub> and impurity. The present model does not contain any source or sink term. The governing equations specified to the three-component (CO<sub>2</sub>, N<sub>2</sub>/SO<sub>2</sub>, H<sub>2</sub>O) aqueous phase model can be written as follows:

$$\frac{\partial}{\partial t} \int_G \phi \rho_o x_i dG - \int_\Gamma (\rho_o \mathbf{v} x_i) \cdot \mathbf{n} d\Gamma + \int_\Gamma (\phi D \rho_o \nabla x_i) \cdot \mathbf{n} d\Gamma = 0, \quad i = 1, 3 \quad (5)$$

$$\mathbf{v} = -\frac{\mathbf{K}}{\mu} (\nabla P - \rho \mathbf{g}) \quad (6)$$

with the supplementary constraints:

$$\sum_{i=1}^3 x_i = 1 \quad (7)$$

**Table 4**  
Injected gas and dissolved gas compositions.

Injected gas compositions (mol%)	Dissolved gas compositions		
	CO <sub>2</sub> (mol%)	N <sub>2</sub> (mol%)	SO <sub>2</sub> (mol%)
100% CO <sub>2</sub>	2.0942 × 10 <sup>-2</sup>	–	–
98% CO <sub>2</sub> + 2% N <sub>2</sub>	2.0469 × 10 <sup>-2</sup>	3.6344 × 10 <sup>-5</sup>	–
95% CO <sub>2</sub> + 5% N <sub>2</sub>	1.9814 × 10 <sup>-2</sup>	7.8986 × 10 <sup>-5</sup>	–
90% CO <sub>2</sub> + 10% N <sub>2</sub>	1.8765 × 10 <sup>-2</sup>	1.3730 × 10 <sup>-4</sup>	–
98% CO <sub>2</sub> + 2% SO <sub>2</sub>	2.0948 × 10 <sup>-2</sup>	–	2.0706 × 10 <sup>-3</sup>
95% CO <sub>2</sub> + 5% SO <sub>2</sub>	2.0940 × 10 <sup>-2</sup>	–	5.1414 × 10 <sup>-3</sup>
90% CO <sub>2</sub> + 10% SO <sub>2</sub>	2.0944 × 10 <sup>-2</sup>	–	1.0185 × 10 <sup>-2</sup>

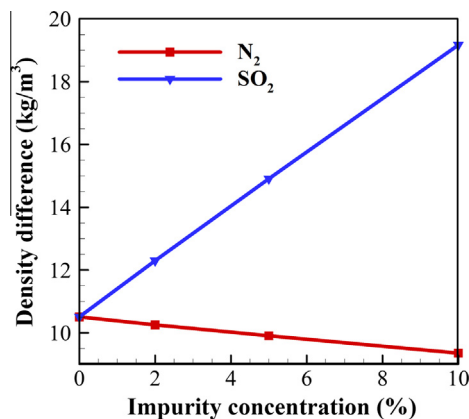


**Fig. 2.** Variations of density difference  $\Delta\rho$  with different N<sub>2</sub> and SO<sub>2</sub> mole percentages.

**Table 5**  
Raleigh numbers for different cases.

Injected gas compositions	Rayleigh number
100% CO <sub>2</sub>	2889.5
98% CO <sub>2</sub> + 2% N <sub>2</sub>	2820.8
95% CO <sub>2</sub> + 5% N <sub>2</sub>	2724.5
90% CO <sub>2</sub> + 10% N <sub>2</sub>	2573.3
98% CO <sub>2</sub> + 2% SO <sub>2</sub>	3381.6
95% CO <sub>2</sub> + 5% SO <sub>2</sub>	4099.2
90% CO <sub>2</sub> + 10% SO <sub>2</sub>	5270.4

$$\frac{M}{\rho} = \frac{x_w M_w}{\rho_w} + \sum_{i=1}^2 V_i x_i \quad (8)$$

The last equation is used to calculate the aqueous phase density by taking into consideration the effects of dissolved gases [31]. The partial molar volume of CO<sub>2</sub> is formulated as a function of temperature [32] while that of N<sub>2</sub> is expressed as a polynomial fit of both temperature and pressure [33]. The SUPCRT92 code is adopted to compute the partial molar volume of SO<sub>2</sub> [34].

### 2.3. Initial and boundary conditions

Initially, the formation water in the simulation domain is assumed to be motionless and no gas is dissolved. As mentioned in Section 2.2, the top boundary is represented as gas-saturated formation water. For the length of the simulation time, the supercritical CO<sub>2</sub> mixtures are supposed to be abundant to keep the aqueous phase at the top boundary saturated with dissolved gases. In order to investigate the sensitivity of the solubility trapping mechanism to different N<sub>2</sub> and SO<sub>2</sub> levels, seven sets of injected gas compositions are chosen, as listed in Table 4. The upper limit of N<sub>2</sub> concentration is chosen to be 10% because the possible mole fraction of N<sub>2</sub> in the captured CO<sub>2</sub> streams is up to that level [13]. The concentrations of SO<sub>2</sub> in the CO<sub>2</sub> streams are generally lower than 10%. However, in order to compare and analyze the effects of the two different non-CO<sub>2</sub> species at equal concentrations, the same initial feed gas compositions are adopted for N<sub>2</sub> and SO<sub>2</sub>. Assuming local thermodynamic equilibrium, the equilibrium

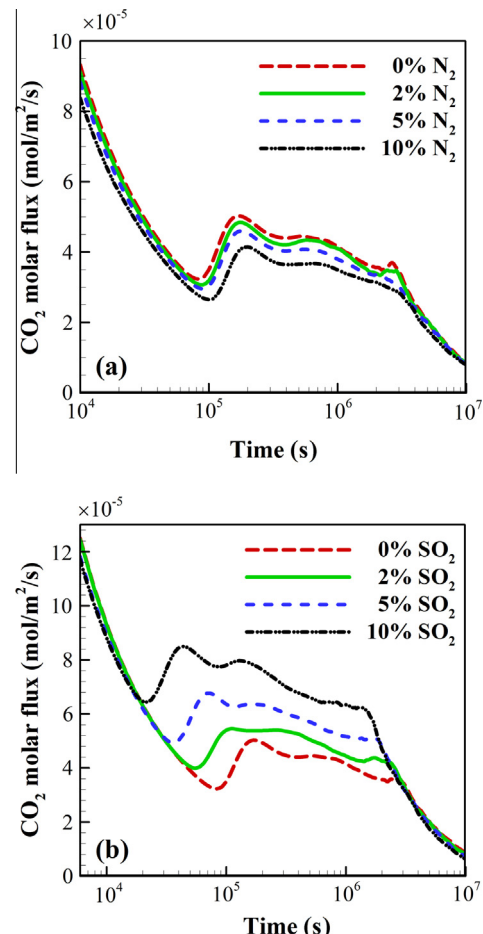


**Fig. 3.** Variations of CO<sub>2</sub> molar fluxes at the top boundary with (a) N<sub>2</sub> and (b) SO<sub>2</sub> mole fractions in the range of 0–10%.

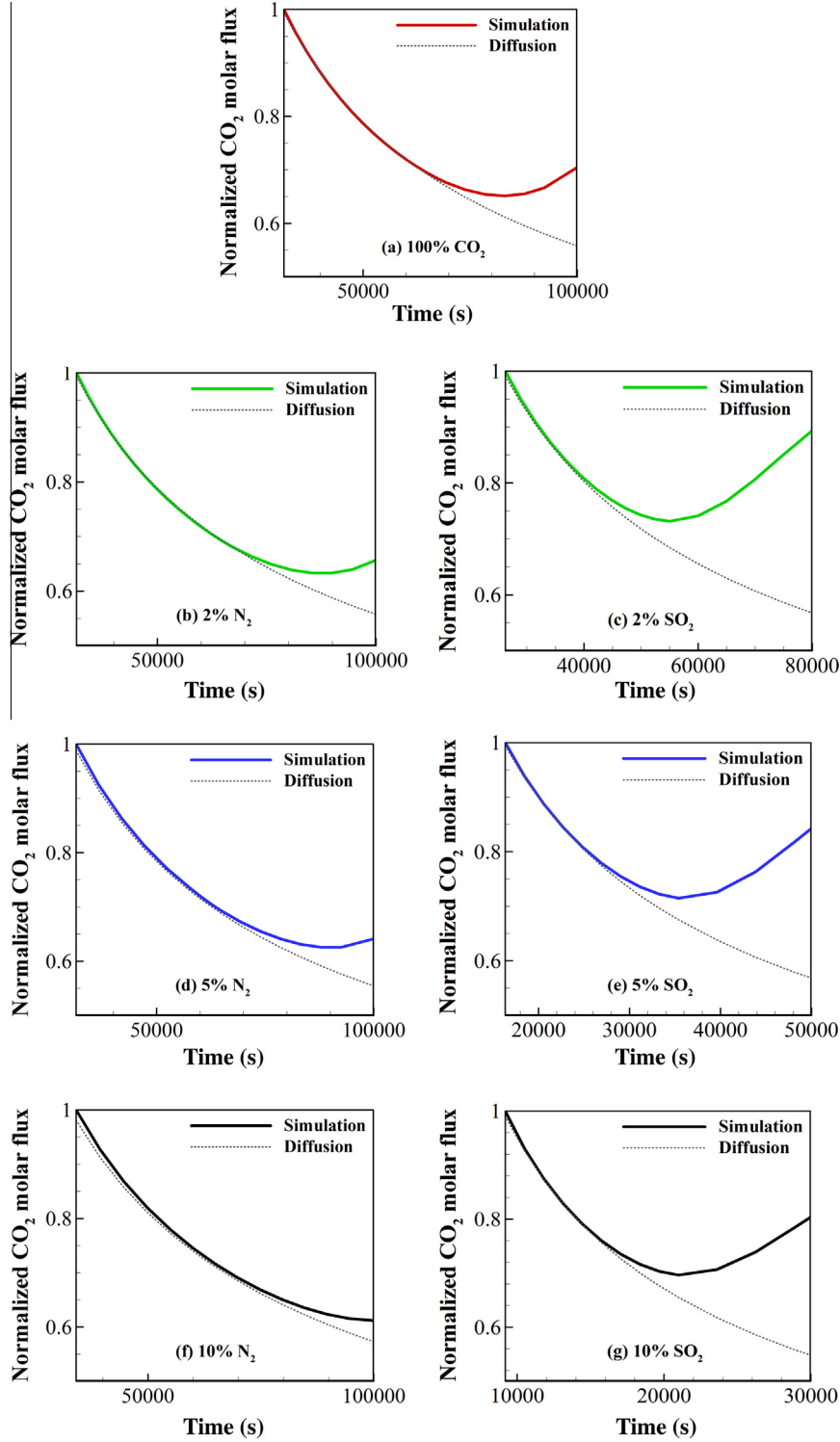


**Fig. 4.** Normalized fluxes from the simulation and pure diffusion (analytical) at different N<sub>2</sub> and SO<sub>2</sub> mole fractions.

compositions can be obtained from flash calculation between the supercritical phase and aqueous phase. The Rachford–Rice equation [35] is adopted to calculate the partitioning of the three components into two phases:

$$\sum_i \frac{z_i(K_i - 1)}{1 + b(K_i - 1)} = 0 \quad (9)$$

Spycher's correlation [36] is employed to obtain the equilibrium constant of water. For CO<sub>2</sub> and the two impurity species, formulations as a function of temperature, pressure and compositions are adopted [37]. The above Rachford–Rice equation can be solved iteratively using either the Newton's method or the bisection method. The mole fractions of both phases can be obtained from the solution *b* of the Rachford–Rice equation as:

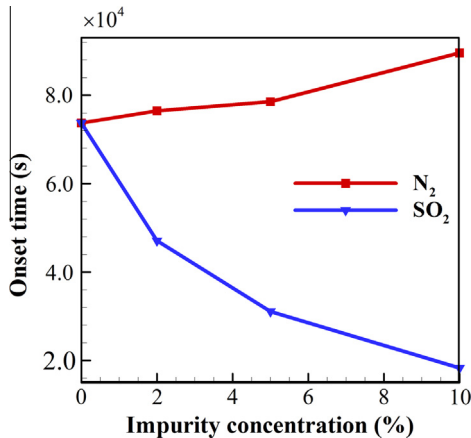


**Fig. 5.** Variations of onset time with different  $N_2$  and  $SO_2$  concentrations in the  $CO_2$  streams.

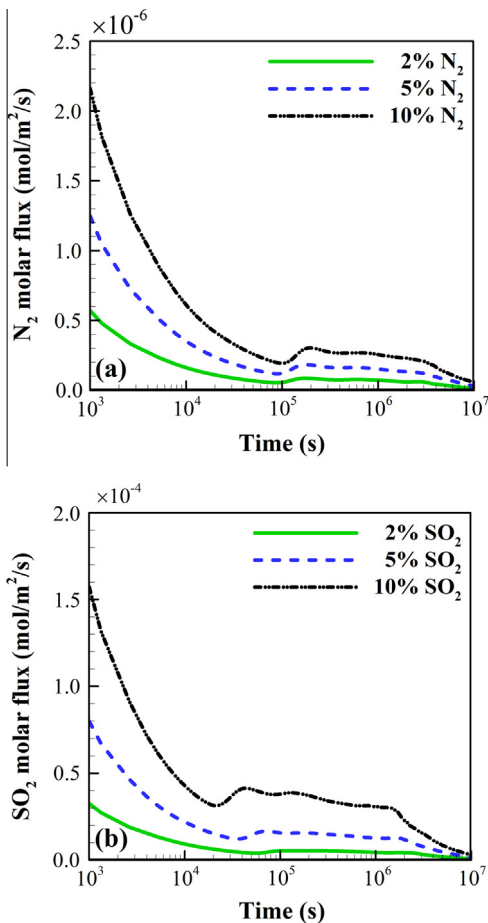


**Fig. 6.** Variations of (a)  $N_2$  impurity dissolution rates and (b)  $SO_2$  impurity dissolution rates.

$$x_i = \frac{z_i}{1 + b(K_i - 1)} \quad (10)$$

$$y_i = K_i x_i \quad (11)$$

Corresponding to the seven sets of injected gas compositions, seven sets of dissolved gas compositions are obtained (Table 4), which will be used as different top boundary conditions. No-flux

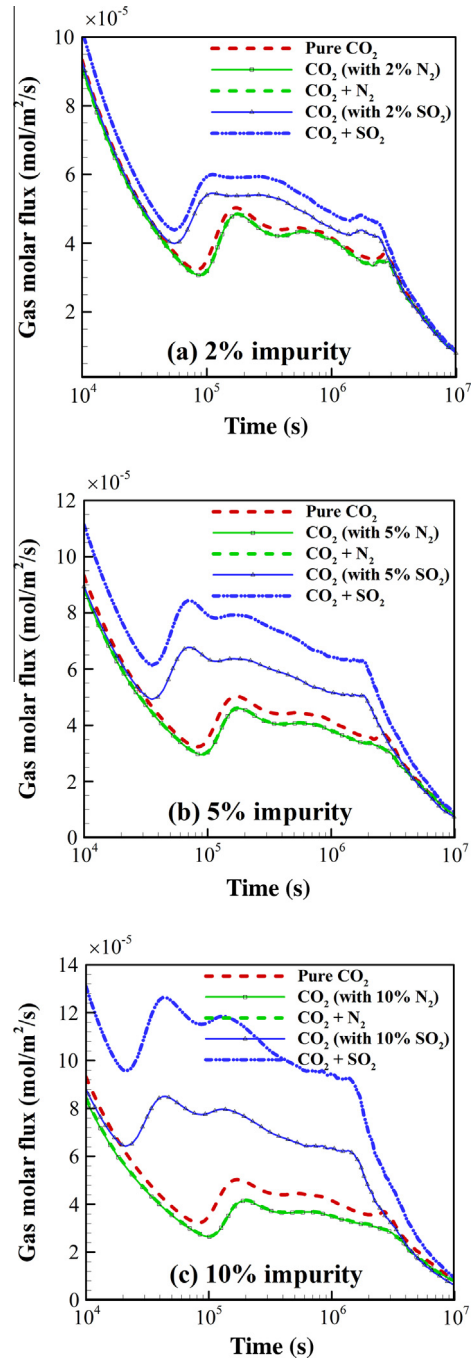


**Fig. 7.** Total molar fluxes of gas for (a) 2%, (b) 5% and (c) 10% impurity concentration cases, respectively. The thinner solid lines with symbols are for the corresponding  $CO_2$  molar fluxes.

boundary conditions are imposed on all the other boundaries (Fig. 1b), which means that there is no fluid flux flowing across these boundaries. The Rayleigh instabilities are generally triggered by geological heterogeneity and/or fluid heterogeneity [38]. Since reservoir permeabilities of most real aquifer formations are heterogeneous, the formation permeabilities of all the grid blocks are disturbed with small random perturbations in the simulations to partially represent the real reservoirs. The equation used in our investigations for the calculation of the scaling factor  $f$  is given as follows:

$$f = m^* 0.08 + 0.96 \quad (12)$$

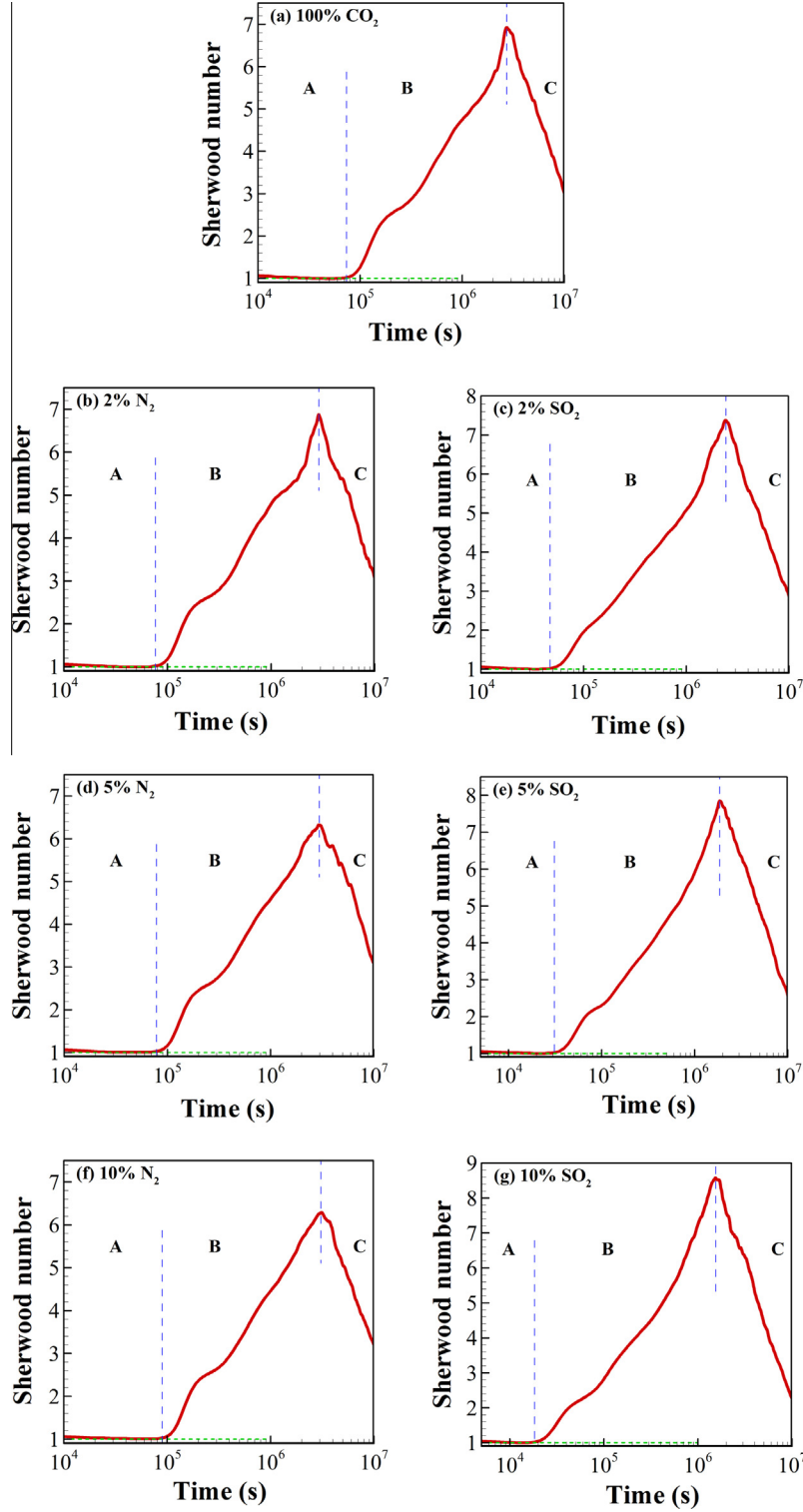


**Fig. 8.** Variations of the Sherwood number with time for different gas composition cases.

By multiplying the scaling factor with the permeability for each grid, a permeability field with random variations of  $\pm 4\%$  amplitude will be obtained. To avoid direct convection from the top boundary and make sure that the fluid transport from the top boundary to the simulation domain occurs only by molecular diffusion, the top boundary is assigned with a rather small permeability.

#### 2.4. Numerical method

Cartesian grid is employed to implement the numerical discretization of the governing equations. The grid spacing in the vertical direction is non-uniform. The grid sizes near the top boundary are chosen to be smaller than the thickness of the diffusive boundary layer [24], while in the lower part of the domain, larger sizes are

used to achieve computational efficiency. In the other two directions, the domain is partitioned uniformly and the grid sizes are chosen to be smaller than the critical wavelength [24,26].

The spatial discretization of the time derivative term employs the integrated finite difference method [39]. For any grid block  $m$ , the time derivative term can be discretized as follows:

$$\frac{\partial}{\partial t} \int_{G_m} \phi \rho_o x_i dG_m = \frac{\partial}{\partial t} [\phi_m \rho_{o,m} x_{i,m} G_m] \quad (13)$$

The discretization of the surface integral of the convective and diffusive fluxes are as follows:

$$\int_{\Gamma_m} (\rho_o \mathbf{v} x_i) \cdot \mathbf{n} d\Gamma_m = \sum_n \rho_{o,mn} v_{mn} x_{i,mn} \Gamma_{mn} \quad (14)$$

with

$$v_{mn} = -\frac{K_{mn}}{\mu_{mn}} \left[ \frac{P_m - P_n}{D_{mn}} - \rho_{mn} g \cos \gamma \right] \quad (15)$$

and

$$\int_{\Gamma_m} (\phi D \rho_o \nabla x_i) \cdot \mathbf{n} d\Gamma_m = \sum_n \phi_m D_m \rho_{o,mn} \nabla x_{i,mn} \Gamma_{mn} \quad (16)$$

The spatial discretization of the governing equations results in a system of ordinary differential equations, which can be discretized using an implicit finite difference method:

$$\begin{aligned} & \left( \phi_m^{t+\Delta t} \rho_{o,m}^{t+\Delta t} x_{i,m}^{t+\Delta t} - \phi_m^t \rho_{o,m}^t x_{i,m}^t \right) \cdot \frac{G_m}{\Delta t} - \sum_n \rho_{o,mn}^{t+\Delta t} v_{mn}^{t+\Delta t} x_{i,mn}^{t+\Delta t} \Gamma_{mn} \\ & + \sum_n \phi_m^{t+\Delta t} D_m^{t+\Delta t} \rho_{o,mn}^{t+\Delta t} \nabla x_{i,mn}^{t+\Delta t} \Gamma_{mn} \\ & = 0, i = 1, 3 \end{aligned} \quad (17)$$

The above strongly nonlinear algebraic equations are linearized using the Newton–Raphson method. To solve the problem accurately, the simulations are started with a rather small time step and an automatic time stepping algorithm is employed to solve the balance equations effectively [40].

### 3. Results and discussion

The density-driven convective mixing problem is similar to the temperature-driven natural convection. In analogy to the thermal Rayleigh number [41], the Rayleigh number  $Ra$  in the density-driven convection is an important non-dimensional parameter, which can be defined as [e.g., 25,27].

$$Ra = \frac{K \Delta \rho g H}{\phi D \mu} \quad (18)$$

where  $\Delta \rho$  stands for the density difference between the gases-saturated liquid and the initial formation water. The dimensionless number  $Ra$  implies the ratio of the convective rate to the diffusive rate [42]. It is indicated that the system remains stable unless the Rayleigh number is greater than the critical Rayleigh number,  $4\pi^2$  [25,43]. Different compositions of the  $CO_2$  streams will result in different density changes. According to Eq. (8) and Table 4, variations of the density differences with different gas compositions at 318.15 K and  $1 \times 10^7$  Pa can be obtained (Fig. 2). For all seven cases, the Rayleigh numbers calculated are much greater than  $4\pi^2$  (Table 5). The effect of the convective mixing on the solubility trapping mechanism is related to the Rayleigh number [44]. Consequently, the changes of the gas compositions are expected to have an impact on the convection process. In the following sections, the impacts of different  $N_2$  and  $SO_2$  concentrations on the onset time and decay time of the instability, the nonlinear fingering dynamics and the other important indicators, such as the

dissolution rate and the total inventory dissolved in the formation fluids, are investigated and presented.

#### 3.1. Onset time and dissolution rate

The onset time is used to characterize the time when the convection begins to turn into a dominant transport mechanism. In this sense, the time when convection occurs determines the efficiency of the solubility trapping mechanism. Linear stability analysis suggests that the onset time can be determined from the following formulation [24]:

$$t_{\text{onset}} = c_0 \frac{\mu^2 \phi^2 D}{(\Delta \rho)^2 g^2 K^2} \quad (19)$$

It should be noted that there is not a definite value of the constant  $c_0$ . Once  $c_0$  is decided, i.e., the definition of the onset time is chosen, it is the density difference  $\Delta \rho$  that makes the onset time different. The density differences for all the gas compositions are positive (Fig. 2), but the density increase decreases with increasing  $N_2$  concentrations while increases with increasing  $SO_2$  concentrations. Furthermore, the magnitude of the density changes of the  $SO_2$  impurity cases is much larger than that of the  $N_2$  impurity cases. It is predicted from Eq. (19) that the occurrence of the instability will take more time for the higher  $N_2$  mole fraction cases. The  $SO_2$  impurity, however, is positive to the occurrence of convection and the extent of the advancement will be larger than that of the delay of the  $N_2$  impurity cases.

In the simulation, the onset time is defined as the time when the dissolution rate, i.e., the simulated molar flux of  $CO_2$  from the top boundary to the simulation domain, is 2% higher than that obtained from the pure diffusive process. Fig. 3 shows the variations of the simulated  $CO_2$  molar fluxes at the top boundary with different  $N_2$  and  $SO_2$  impurity concentrations. To obtain the onset time, Fig. 4 then compares the normalized simulated fluxes and diffusive fluxes for the seven cases. At the early times, the diffusive fluxes in Fig. 4d and f are a little lower than the corresponding simulated fluxes. The deviations may be attributed to the equations of state adopted, especially the binary interaction coefficients [45,46]. The fluxes then agree quite well with each other after about 5000 s. Fig. 5 is the result of the sensitivity of onset time to the variations of  $N_2$  and  $SO_2$  concentration levels. According to the onset time obtained for the pure  $CO_2$  case,  $c_0$  calculated in this simulation is about 1231, which falls in the range predicted by previous studies [29]. With increasing  $N_2$  concentrations in the initial gas mixtures and thus increasing dissolved  $N_2$  concentrations, the onset time increases, which is consistent with the trend predicted by Eq. (19). The inclusion of  $N_2$  in the  $CO_2$  streams delays the onset time of the convection, which is negative to the dissolution of  $CO_2$  and the solubility trapping mechanism. For the  $SO_2$  impurity, the onset time decreases with increasing  $SO_2$  concentrations. Furthermore,  $SO_2$  has more prominent impact on the onset time than  $N_2$  at the same impurity concentration.

The dissolution rate of  $CO_2$  is an important indicator of the solubility trapping mechanism. As shown in Fig. 3, the evolution of

**Table 6**

The maximum Sherwood number and the decay time.

Injected gas compositions	Maximum Sherwood number	Decay time (s)
100% $CO_2$	6.92	$2.7370 \times 10^6$
98% $CO_2$ + 2% $N_2$	6.87	$2.8936 \times 10^6$
95% $CO_2$ + 5% $N_2$	6.32	$2.9693 \times 10^6$
90% $CO_2$ + 10% $N_2$	6.29	$3.0591 \times 10^6$
98% $CO_2$ + 2% $SO_2$	7.38	$2.4247 \times 10^6$
95% $CO_2$ + 5% $SO_2$	7.85	$1.8533 \times 10^6$
90% $CO_2$ + 10% $SO_2$	8.58	$1.5407 \times 10^6$

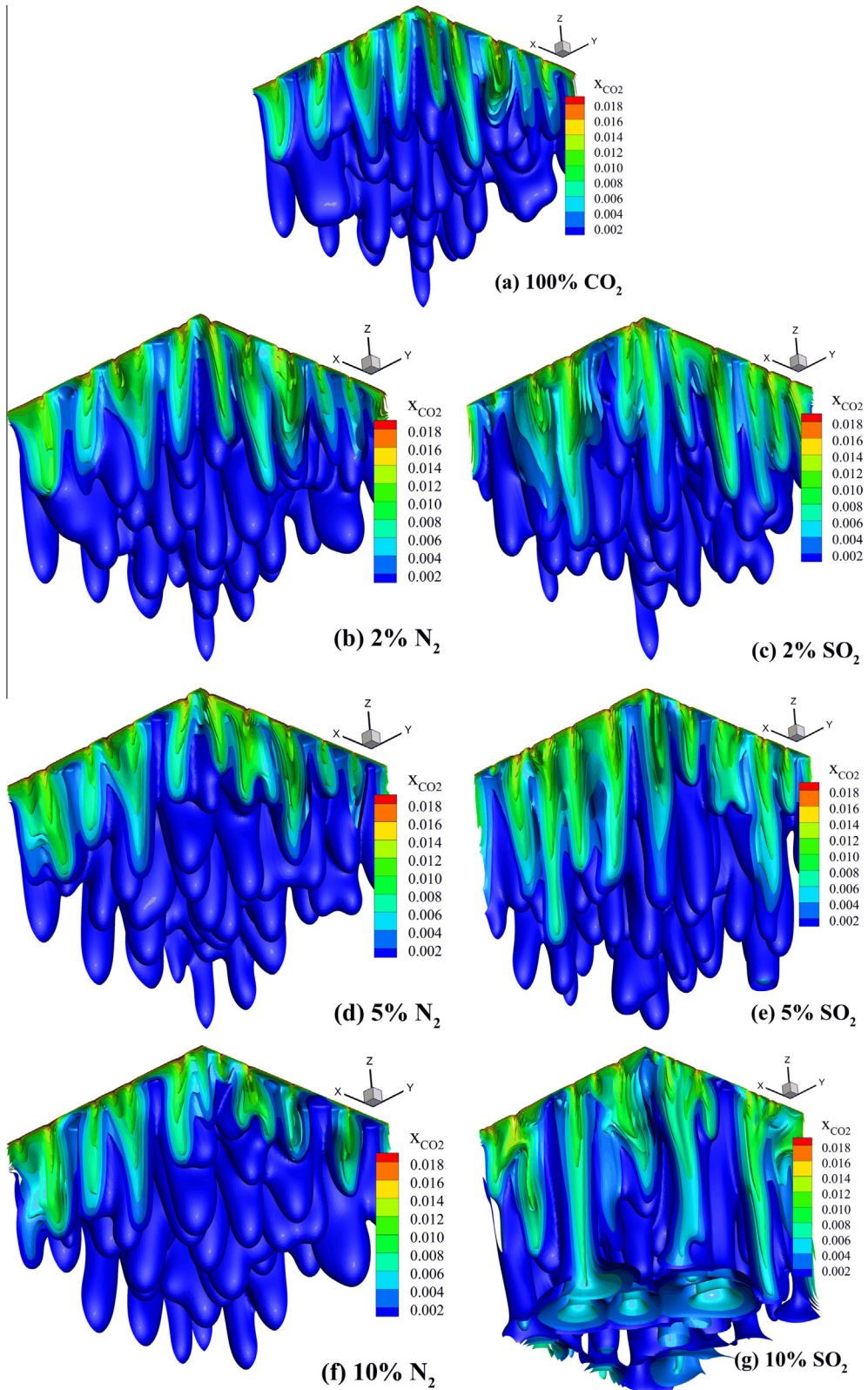


**Fig. 9.** Simulated CO<sub>2</sub> distributions at  $t = 1.0 \times 10^6$  s for different N<sub>2</sub> and SO<sub>2</sub> concentrations.

the dissolution rates can be roughly divided into three periods: the diffusion-dominated period, the convection-dominated period and the decay of the convection period. Before the occurrence of convection, the downward transport of dissolved gases is dominated

by molecular diffusion and the dissolution rates decrease with time as  $t^{-0.5}$ . During the diffusion-dominated period, different kinds of non-CO<sub>2</sub> species have insignificant effects on the dissolution rates. The increase of N<sub>2</sub> concentration reduces the dissolution

rates at this stage, but the effects are quite small (Fig. 3a). During the convection-dominated period, the effects of impurities on the dissolution rates are much bigger than that during the diffusion-dominated process. It is obvious that the inclusion of the  $N_2$  impurity decreases the dissolution rate while the inclusion of the  $SO_2$  impurity accelerates the dissolution rate. The magnitude of the change of the dissolution rates for the  $CO_2-SO_2$  cases is much larger than that of the  $CO_2-N_2$  cases at the same impurity concentration. Since the convective mixing in the  $SO_2$  cases is more intense, the concentration fronts will reach the bottom boundary earlier. Then the upward moving liquids contain more dissolved gases and the driving force of the convection, i.e., the density gradient, decays and the molecular diffusion becomes the dominant transport process again. The dissolution rates decrease correspondingly. The differences of the dissolution rates between different gas composition cases are rather small during the last period.

The dissolution rates of the impurities are also important, especially for the hazardous  $SO_2$ . Once dissolved into the formation fluids, the possibility of leakage is reduced. Fig. 6 shows the dissolution rates of the co-injected  $N_2$  and  $SO_2$ . The dissolution rates of the two impurities share similar trend with the  $CO_2$  dissolution rates. The dissolution rates of the  $SO_2$  impurity are almost two orders of magnitude higher than that of the corresponding  $N_2$  impurity. The higher the impurity concentration, the faster the dissolution for both impurities. During the convection-dominated period, the fluctuations of the  $N_2/SO_2$  dissolution rates are smaller than that of the  $CO_2$  dissolution rates. Fig. 7 displays gas dissolution rates for the chosen impurity concentrations. The thinner solid lines with symbols are the  $CO_2$  molar fluxes at corresponding impurity contents. The curves of  $CO_2$  and  $N_2$  total molar fluxes almost overlap with that of the corresponding  $CO_2$  molar fluxes. The results imply that the dissolution of  $N_2$  is insignificant compared to the dissolution of  $CO_2$ . The dissolution rates of the  $CO_2$  and  $SO_2$  mixture, however, increase obviously even for the 2%  $SO_2$  concentration case.

### 3.2. Decay of convection

The diffusion-dominated period and convection-dominated period can be distinguished by the onset time of convection. However, the time when the decay of convection begins is not clearly illustrated yet. The Sherwood number represents the ratio of total mass transfer to diffusive mass transfer [47]. Previous study [48] indicated that the maximum Sherwood number could be used to characterize the decay of convection. Fig. 8 shows the variations of the Sherwood numbers with time for different gas composition cases. The evolution of the Sherwood number can also be divided into three phases, corresponding to the three periods of the dissolution rate. The left vertical dashed lines correspond to the onset time of convection for all cases. In phase A, the Sherwood number remains unity, which confirms that the dominant mass transfer mechanism is pure diffusion. In phase B, the Sherwood number increases with time since the convective mixing becomes the primary mass transfer mechanism. Once the upward moving fluids contain sufficient dissolved gases after the leading fingers have reached the bottom boundary, the dissolution rate decreases and the Sherwood number will decrease accordingly. The maximum Sherwood number obtained for different cases and the decay time are listed in Table 6. It can be concluded that the maximum Sherwood number decreases with increasing  $N_2$  concentrations while increases with increasing  $SO_2$  concentrations. The larger the maximum Sherwood number, the more intense the convection and the earlier the leading fingers reaching the bottom boundary. Consequently, the trend of the decay time contrasts to the variation of the maximum Sherwood number.

### 3.3. Nonlinear behavior

The convective mixing is rather chaotic in nature and it is hard to quantify the effects of impurities on the convection process. In this study, the sensitivity of the convection process to  $N_2$  and  $SO_2$  impurity is demonstrated through the comparisons of the dissolved  $CO_2$  distributions. First, the snapshots of  $CO_2$  concentrations at  $t = 1.0 \times 10^6$  s are compared (Fig. 9). It is indicated that both the impurity species and their concentrations can have an effect upon the formation and development of the fingers. The finger distributions, including the fingers near and at the side boundaries, as well as the preferential flow paths [27] of the seven cases differ from each other. The convection in the pure  $CO_2$  case is stronger than that in the  $N_2$  impurity cases but weaker than that in the  $SO_2$

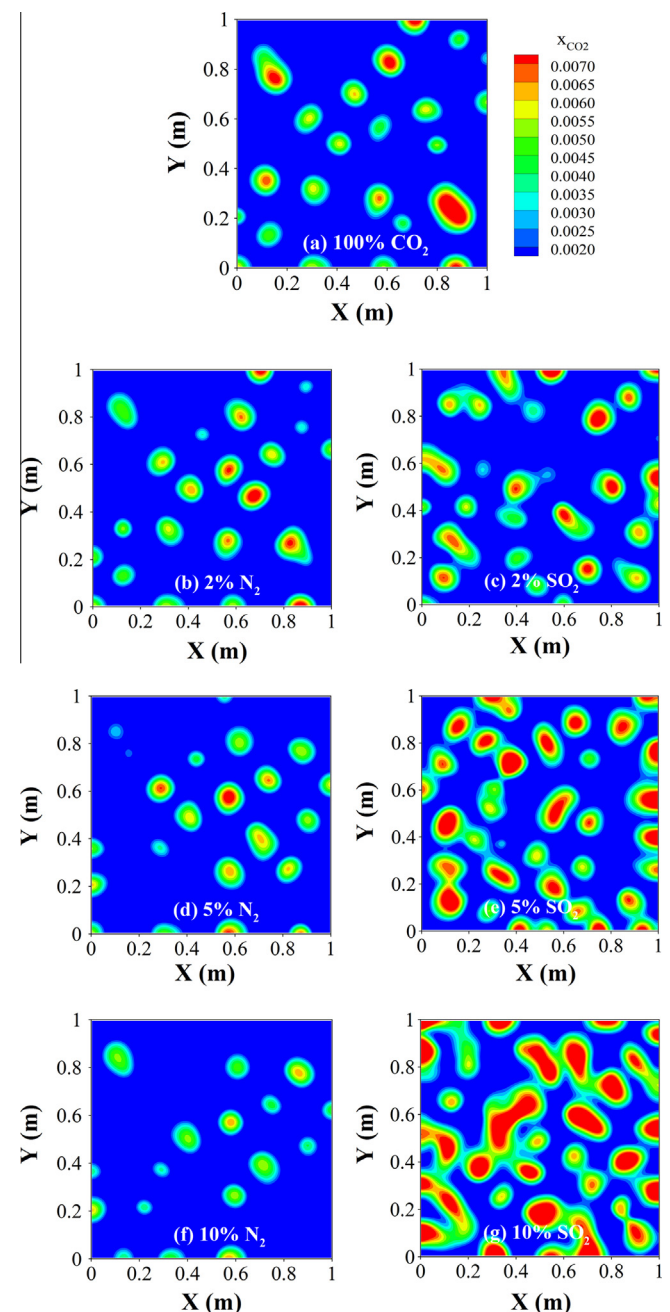
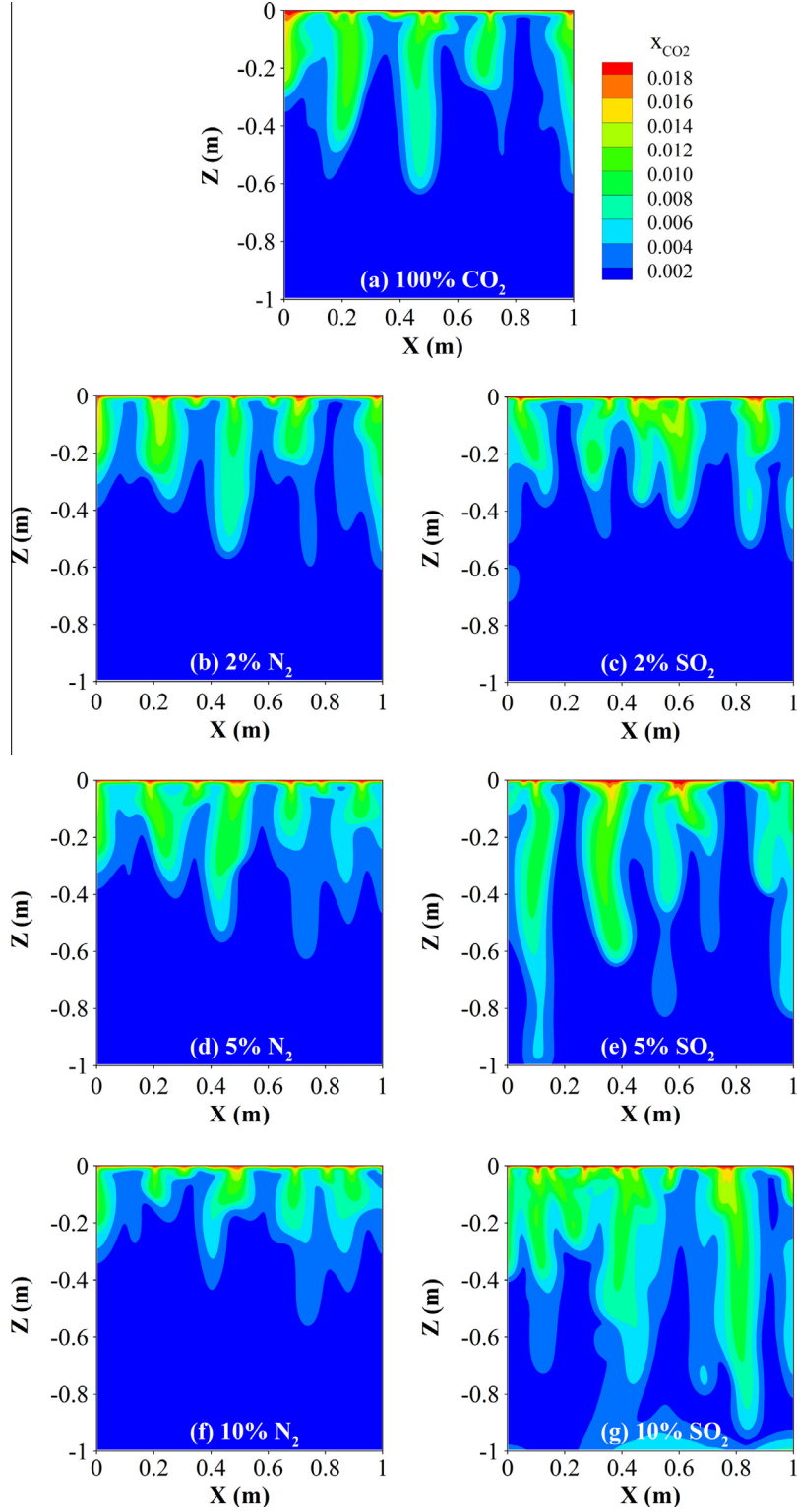


Fig. 10. Cross-sections in the XY-plane along  $Z = -0.575$  m at  $t = 1.0 \times 10^6$  s.



**Fig. 11.** Cross-sections in the XZ-plane along  $Y = 0.695$  m at  $t = 1.0 \times 10^6$  s.

impurity cases. According to Hassanzadeh et al. [48], the maximum velocity in the vertical direction is proportional to the density difference  $\Delta\rho$ . Since the higher the  $N_2$  mole fraction, the smaller the density difference, the leading fingers in the higher  $N_2$  concentration cases will not transport as far as that in the lower  $N_2$  concentration cases, as proved in Fig. 9. The effect of  $SO_2$  on the downward

transport of concentration fingers is opposite to that of  $N_2$ . Furthermore, the change of the finger distributions is more marked for the  $SO_2$  cases at the same impurity concentration. It should be noted that the fastest fingers in Fig. 9e and g have reached the bottom boundary at  $t = 1.0 \times 10^6$  s, which is earlier than the decay time (Table 6). This is because the concentrations of dissolved gases

contained in the upward moving fluids are not very high at this specific time and convection remains the dominant mass transfer mechanism.

Although the 3D isosurfaces of the dissolved CO<sub>2</sub> concentrations intuitively demonstrate the structures of the fingers, comparisons of the contour plots in the XY-plane, XZ-plane and YZ-plane of the 3D solution need to be made to highlight the

internal details of the fingers. Corresponding to  $t = 1.0 \times 10^6$  s, Figs. 10–12 are the cross-sectional contours in the planes along  $Z = -0.575$  m,  $Y = 0.695$  m and  $X = 0.2$  m, respectively. It can be seen from these figures that the dissolved CO<sub>2</sub> concentrations are generally higher when the N<sub>2</sub> mole fractions are lower or when the SO<sub>2</sub> mole fractions are higher. The changes of dissolved CO<sub>2</sub> concentration distributions in the SO<sub>2</sub> cases are more

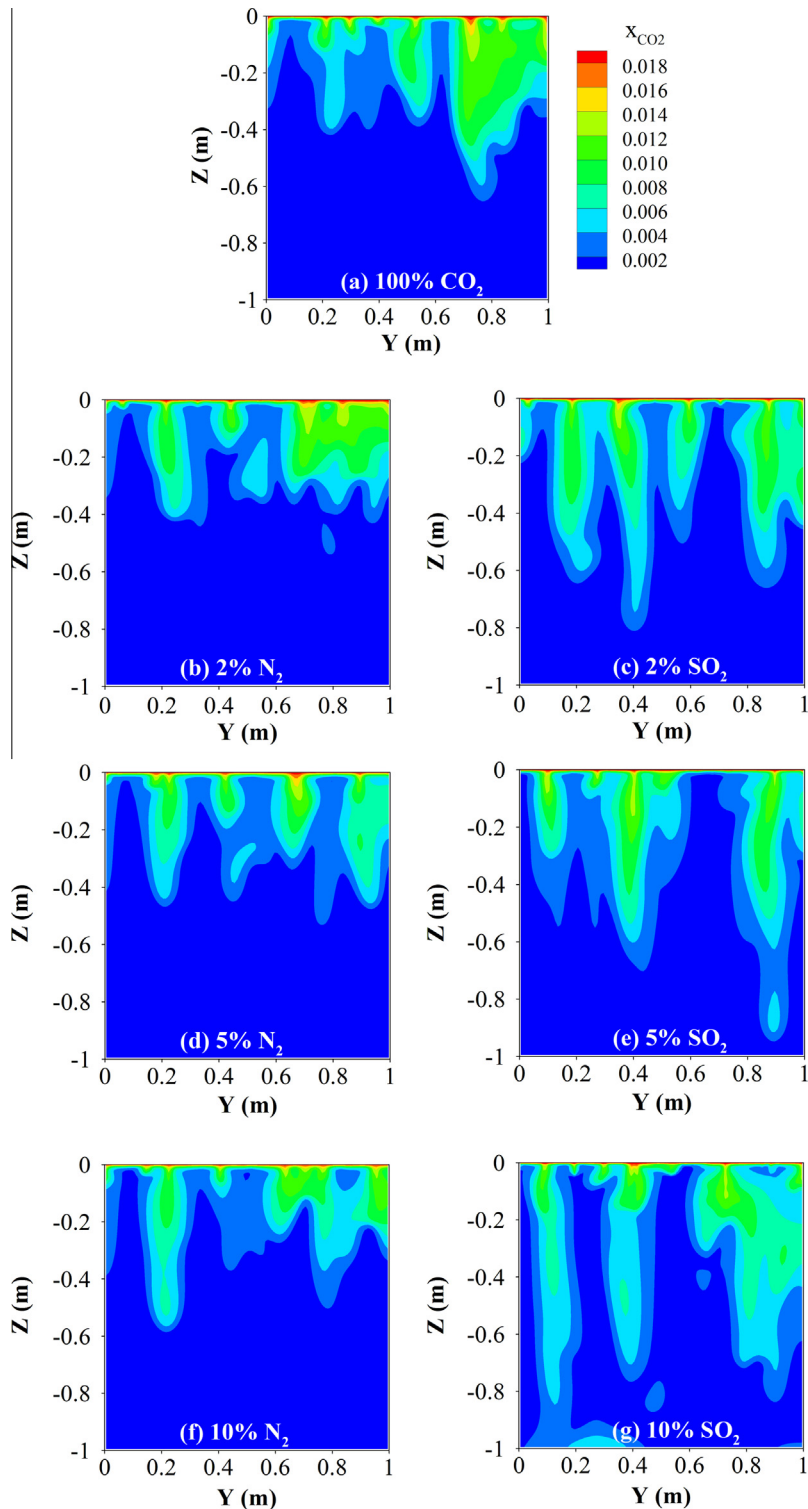
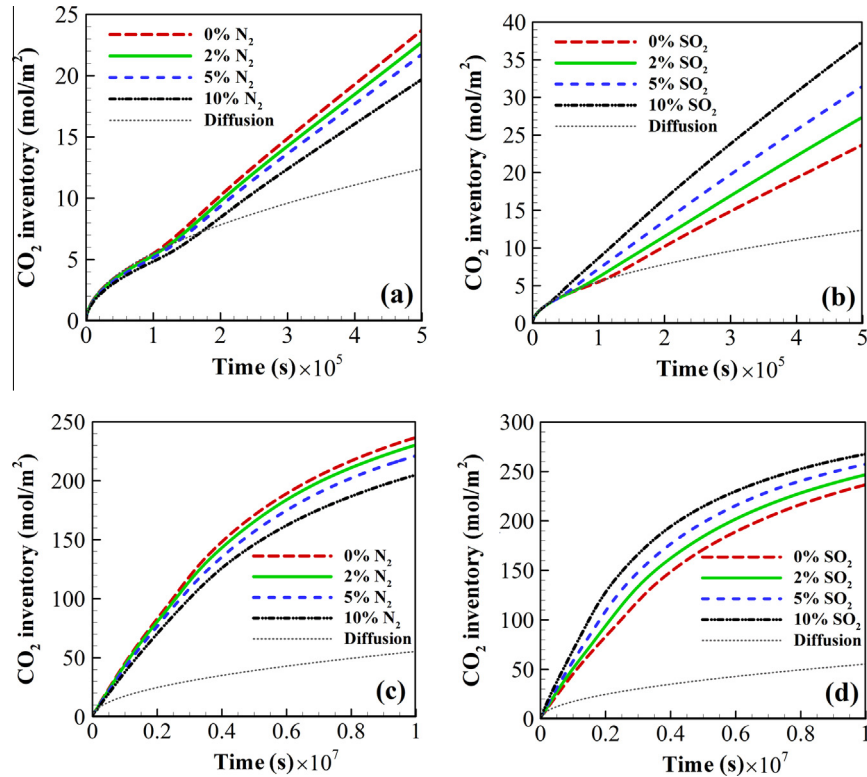


Fig. 12. Cross-sections in the YZ-plane along  $X = 0.2$  m at  $t = 1.0 \times 10^6$  s.



**Fig. 13.** Variations of the dissolved  $\text{CO}_2$  inventory with different  $\text{N}_2$  and  $\text{SO}_2$  concentrations. The top two figures are for the early stage and the bottom two figures are for the length of the simulation time.

marked. The high-concentration profiles in Fig. 10 confirm that the preferential flow paths are affected by the type of the impurities and the change of the impurity concentrations. The numbers of fingers that have reached the same XY-plane at  $t = 1.0 \times 10^6$  s differ from different cases.

#### 3.4. Total inventory

Despite the chaotic nature of the convection process, total inventory dissolved in the formation fluids are rather robust. Fig. 13 demonstrates the variations of the total dissolved  $\text{CO}_2$  inventories with different  $\text{N}_2$  and  $\text{SO}_2$  mole fractions. The thinner dashed curves, representing  $\text{CO}_2$  inventory transported by pure diffusion, are calculated for the pure  $\text{CO}_2$  case. It can be seen that for the pure  $\text{CO}_2$  case, the amount of  $\text{CO}_2$  dissolved in the formation fluids obtained from the numerical simulation is consistent with that calculated from the analytical diffusive process until about  $1.15 \times 10^5$  s. As the convective process accelerates the dissolution rate greatly, the total inventory of  $\text{CO}_2$  increases compared with that of the diffusive process. The amount of dissolved  $\text{CO}_2$  is generally linear with time during the convection-dominated period, which indicates that the dissolution rate of  $\text{CO}_2$  is approximately stable during this stage. With increasing  $\text{N}_2$  concentration, the total dissolved  $\text{CO}_2$  inventory decreases. Since the inclusion of the  $\text{SO}_2$  impurity is positive to the convective mixing, the total dissolved  $\text{CO}_2$  inventory is larger in the higher  $\text{SO}_2$  concentration case. Fig. 14 shows the total dissolved gas inventories for different impurity concentrations. The inclusion of the  $\text{N}_2$  impurity decreases the total dissolved gas inventory while the inclusion of the  $\text{SO}_2$  impurity increases it. The total dissolved  $\text{CO}_2$  and  $\text{N}_2$  inventory is almost equal to the corresponding dissolved  $\text{CO}_2$  inventory, implying that the dissolved

$\text{N}_2$  inventory can be neglected compared to the dissolved  $\text{CO}_2$  inventory. With increasing  $\text{SO}_2$  concentration, the dissolved  $\text{SO}_2$  inventory increases and the total dissolved gas inventory increases accordingly. Table 7 lists dissolved  $\text{CO}_2$  inventories and total dissolved gas inventories for the seven gas composition cases at  $1.0 \times 10^7$  s.

#### 3.5. Comparison with other results

Because of the practical importance to safe  $\text{CO}_2$  storage, the density-driven convective mixing has been widely studied. Here the results of the pure  $\text{CO}_2$  case in our simulations are compared with previous typical investigations where same parameters, including temperature, pressure, formation permeability, porosity, salinity, diffusivity, etc. are adopted [29,49]. Firstly, there is good agreement between the simulated fluxes and the diffusive fluxes obtained by theoretical analysis at the early stage (Fig. 4). In spite of the chaotic nature of the convective processes, the convective flow patterns share similar features compared with previous investigations. The integral measures of the solubility trapping mechanisms, such as the onset time of convection and the dissolution rates as well as the total inventory of  $\text{CO}_2$  into the aqueous phase, are also comparable with previous investigations (note the different units used).

The simulation results obtained may be applied to the Utsira formation, the formation used for the injection of  $\text{CO}_2$  near the Sleipner Field. In spite of different opinions on the depositional environment of this formation, it seems reasonable to believe that the Utsira sandstone was deposited as mass flows or turbidite sands. This kind of sandstone is assumed to have a high porosity and permeability while the vertical to horizontal permeability ratio is approximately 1 [50]. In this sense, our results may serve as ref-

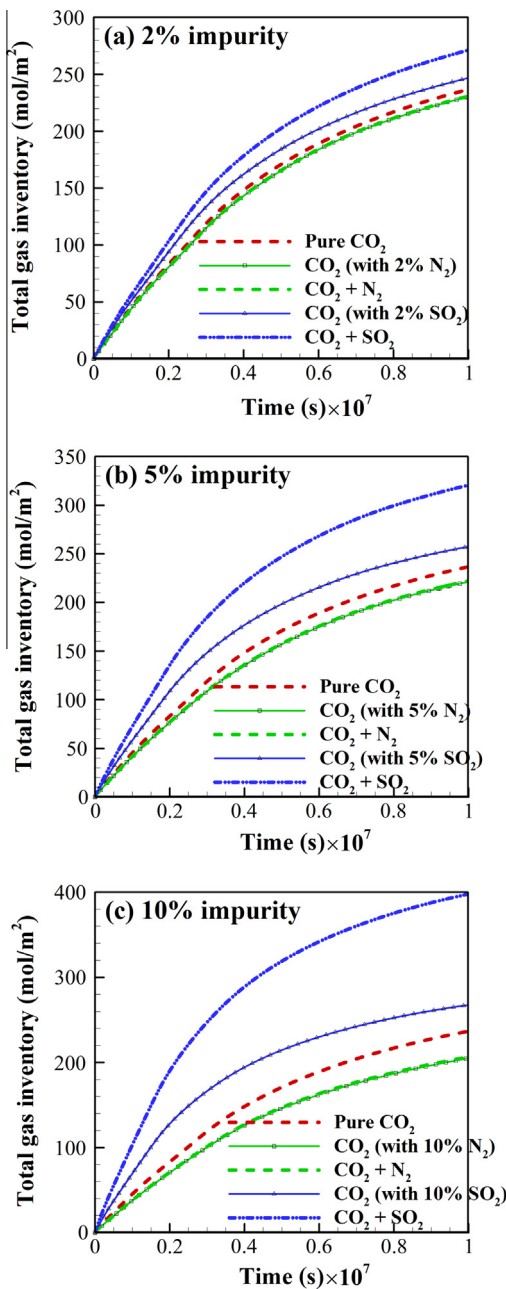


**Fig. 14.** Total dissolved gas inventory for (a) 2%, (b) 5% and (c) 10% impurity concentration cases. The thinner solid lines with symbols are for the corresponding dissolved  $\text{CO}_2$  inventories.

**Table 7**

Total dissolved  $\text{CO}_2$  and gas inventories at  $t = 1.0 \times 10^7$  s.

Injected gas compositions	$\text{CO}_2$ inventory (mol/ $\text{m}^2$ )	Total gas inventory (mol/ $\text{m}^2$ )
100% $\text{CO}_2$	236.74	236.74
98% $\text{CO}_2$ + 2% $\text{N}_2$	230.44	230.85
95% $\text{CO}_2$ + 5% $\text{N}_2$	221.20	222.09
90% $\text{CO}_2$ + 10% $\text{N}_2$	205.05	206.55
98% $\text{CO}_2$ + 2% $\text{SO}_2$	246.84	271.35
95% $\text{CO}_2$ + 5% $\text{SO}_2$	257.44	320.65
90% $\text{CO}_2$ + 10% $\text{SO}_2$	367.68	397.86

erences for the co-injections of  $\text{CO}_2$  and impurities in such kind of formations.

#### 4. Conclusions and future work

Allowing the presence of impurities in the  $\text{CO}_2$  streams is cost-effective for carbon capture, but it may have undesirable effects on transportation and geological storage. In this study, 3D numerical simulations are carried out to evaluate the effects of  $\text{N}_2$  and  $\text{SO}_2$  impurities on the solubility trapping mechanism. When dissolved into the formation water, the co-injected  $\text{N}_2$  is found to reduce the density increase and the corresponding Rayleigh instability. Increasing  $\text{N}_2$  concentration in the injected mixture, the occurrence of convection requires more time. The variation of the  $\text{CO}_2$  and  $\text{N}_2$  compositions also has an impact on the dynamic fingering processes. The convection processes are stronger in the lower  $\text{N}_2$  concentration cases: the fingers form earlier and transport faster than in the higher  $\text{N}_2$  concentration cases. The dissolution rate is higher and there is more  $\text{CO}_2$  dissolved when  $\text{N}_2$  concentration is lower. It implies that the inclusion of  $\text{N}_2$  in the  $\text{CO}_2$  streams is negative to the geological storage. The buoyant and mobile  $\text{CO}_2$  and  $\text{N}_2$  streams are more likely to leak from the storage sites. Allowing the existence of  $\text{N}_2$  requires better risk management for the security of  $\text{CO}_2$  geological storage.  $\text{SO}_2$  is more soluble than  $\text{N}_2$  and is suggested positive to the convective mixing. Furthermore, the magnitude of the effects of  $\text{SO}_2$  impurity is larger than the corresponding  $\text{N}_2$  impurity. It is implied that the inclusion of  $\text{SO}_2$  may be beneficial to the safe storage of  $\text{CO}_2$ . Meanwhile, the hazardous  $\text{SO}_2$  could also be isolated from the atmosphere. However, considering the possible corrosion and acidification of  $\text{SO}_2$  in the long term, the  $\text{SO}_2$  concentration should be chosen carefully in order to balance the positive and opposite effects of  $\text{SO}_2$ .

The present study ignores the salinity effects on the solubility of the gases for simplicity. In the future, the impacts of the salinity on the  $\text{CO}_2$  and impurity convective mixing will be investigated. The effects of  $\text{N}_2$  and  $\text{SO}_2$  are studied separately in our investigations. In the future, the co-injection of  $\text{CO}_2$  and two or more non- $\text{CO}_2$  species will be taken into consideration to obtain a better understanding of the impacts of impurities on CCS.

#### References

- [1] Intergovernmental panel on climate change (IPCC). In: Metz B, Davidson O, de Coninck H, Loos M, Meyer LA, editors. IPCC special report on carbon dioxide capture and storage. Cambridge University Press; 2005.
- [2] Bachu S.  $\text{CO}_2$  storage in geological media: role, means, status and barriers to deployment. *Prog Energy Combust Sci* 2008;34:254–73.
- [3] Wang J, Ryan D, Anthony EJ, Wigston A. Effects of impurities on geological storage of  $\text{CO}_2$ . Report for IEA GHG, 2011.
- [4] Liu H, Shao YJ. Predictions of the impurities in the  $\text{CO}_2$  stream of an oxy-coal combustion plant. *Appl Energy* 2010;87(10):3162–70.
- [5] Knauss KG, Johnson JW, Steefel CI. Evaluation of the impact of  $\text{CO}_2$ , co-contaminant gas, aqueous fluid and reservoir rock interactions on the geologic sequestration of  $\text{CO}_2$ . *Chem Geol* 2005;217:339–50.
- [6] Ji XY, Zhu C. Predicting possible effects of  $\text{H}_2\text{S}$  impurity on  $\text{CO}_2$  transportation and geological storage. *Environ Sci Technol* 2013;47:55–62.
- [7] Nicot J-P, Solano S, Lu J, Mickler P, Romanak K, Yang C, et al. Potential subsurface impacts of  $\text{CO}_2$  stream impurities on geologic carbon storage. *Energy Procedia* 2013;37:4552–9.
- [8] Kather A. Presented at 2nd working group meeting on  $\text{CO}_2$  quality and other relevant issues. Germany: Cottbus; 2009.
- [9] Davidson J, Thambimuthu K. An overview of technologies and costs of carbon dioxide capture in power generation. *Proc Inst Mech Eng, Part A* 2009;223:201–12.
- [10] de Visser E, Hendriks C, Barrio M, Mølnvik MJ, de Koeijer G, Liljemark S, et al. Dynamis  $\text{CO}_2$  quality recommendations. *Int J Greenhouse Gas Control* 2008;2:478–84.
- [11] Huh C, Kang S-G, Cho M-I, Baek J-H. Effects of water and nitrogen impurities on  $\text{CO}_2$  pipeline transport for geological storage. *Energy Procedia* 2011;4:2214–21.
- [12] Chacykowski M, Osiadacz AJ. Dynamic simulation of pipelines containing dense phase/supercritical  $\text{CO}_2$ -rich mixtures for carbon capture and storage. *Int J Greenhouse Gas Control* 2012;9:446–56.
- [13] Li HL, Jakobsen JP, Wilhelmsen Ø, Yan JY. PVTxy properties of  $\text{CO}_2$  mixtures relevant for  $\text{CO}_2$  capture, transport and storage: review of available experimental data and theoretical models. *Appl Energy* 2011;88:3567–79.

- [14] Crandell LE, Ellis BR, Peters CA. Dissolution potential of SO<sub>2</sub> co-injected with CO<sub>2</sub> in geologic sequestration. *Environ Sci Technol* 2010;44:349–55.
- [15] Choi Y-S, Nesic S, Young D. Effect of impurities on the corrosion behavior of CO<sub>2</sub> transmission pipeline steel in supercritical CO<sub>2</sub>-water environments. *Environ Sci Technol* 2010;44:9233–8.
- [16] Dugstad A, Morland B, Clausen S. Corrosion of transport pipelines for CO<sub>2</sub>-effect of water ingress. *Energy Procedia* 2011;4:3063–70.
- [17] Xiang Y, Wang Z, Xu CC, Zhou C, Li Z, Ni WD. Impact of SO<sub>2</sub> concentration on the corrosion rate of X70 steel and iron in water-saturated supercritical CO<sub>2</sub> mixed with SO<sub>2</sub>. *J Supercrit Fluids* 2011;58:286–94.
- [18] Xu TF, Apps JA, Pruess K, Yamamoto H. Numerical modeling of injection and mineral trapping of CO<sub>2</sub> with H<sub>2</sub>S and SO<sub>2</sub> in a sandstone formation. *Chem Geol* 2007;242:319–46.
- [19] Bacon DH, Sass BM, Bhargava M, Sminchak J, Gupta N. Reactive transport modeling of CO<sub>2</sub> and SO<sub>2</sub> injection into deep saline formations and their effect on the hydraulic properties of host rocks. *Energy Procedia* 2009;1:3283–90.
- [20] Bacon DH, Murphy EM. Managing chemistry underground: is co-sequestration an option in selected formations? *Energy Procedia* 2011;4:4457–64.
- [21] Ellis BR, Crandell LE, Peters CA. Limitations for brine acidification due to SO<sub>2</sub> co-injection in geologic carbon sequestration. *Int J Greenhouse Gas Control* 2010;4:575–82.
- [22] Bickle MJ. Geological carbon storage. *Nat Geosci* 2009;2:815–8.
- [23] Jiang X. A review of physical modelling and numerical simulation of long-term geological storage of CO<sub>2</sub>. *Appl Energy* 2011;88(11):3557–66.
- [24] Ennis-King J, Preston I, Paterson L. Onset of convection in anisotropic porous media subject to a rapid change in boundary conditions. *Phys Fluids* 2005;17:084107–15.
- [25] Hassanzadeh H, Pooladi-Darvish M, Keith DW. Modelling of convection mixing in CO<sub>2</sub> storage. *J Can Petrol Technol* 2005;44:43–51.
- [26] Xu XF, Chen SY, Zhang DX. Convective stability analysis of the long-term storage of carbon dioxide in deep saline aquifers. *Adv Water Resour* 2006;29:397–407.
- [27] Hesse MA. Mathematical modeling and multiscale simulation of CO<sub>2</sub> storage in saline aquifers. Stanford University: PhD, Dept. of Energy Resources Engineering; 2008.
- [28] Lu C, Lichtner PC. High resolution numerical investigation on the effect of convective instability on long term CO<sub>2</sub> storage in saline aquifers. *J Phys: Conf Ser* 2007;78:012042.
- [29] Pau GSH, Bell JB, Pruess K, Almgren AS, Lijewski MJ, Zhang K. High-resolution simulation and characterization of density-driven flow in CO<sub>2</sub> storage in saline aquifers. *Adv Water Resour* 2010;33(4):443–55.
- [30] Helmig R. Multiphase flow and transport processes in the subsurface: a contribution to the modeling of hydrosystems. Berlin: Springer; 1997.
- [31] Battistelli A, Marcolini M. TMGAS: a new TOUGH2 EOS module for the numerical simulation of gas mixtures injection in geological structures. *Int J Greenhouse Gas Control* 2009;3:481–93.
- [32] Garcia JE. Density of aqueous solutions of CO<sub>2</sub>. Technical report LBNL-49023, Lawrence Berkeley National Laboratory, California, 2001.
- [33] Mao S, Duan ZH. A thermodynamic model for calculating nitrogen solubility, gas phase composition and density of the N<sub>2</sub>-H<sub>2</sub>O-NaCl system. *Fluid Phase Equilibil* 2006;248:103–14.
- [34] Johnson JW, Oelkers EH, Helgeson HC. SUPCRT92: a software package for calculating the standard molal thermodynamic properties of minerals, gases, aqueous species, and reactions from 1 to 5000 bars and 0 to 1000 °C. *Comput Geosci* 1992;18(7):899–947.
- [35] Rachford HH, Rice JD. Procedure for use of electrical digital computers in calculating flash vaporization hydrocarbon equilibrium. *J Petrol Technol* 1952;4(10):10–9.
- [36] Spycher N, Pruess K, Ennis-King J. CO<sub>2</sub>-H<sub>2</sub>O mixtures in the geological sequestration of CO<sub>2</sub>. I. assessment and calculation of mutual solubilities from 12 to 100 °C and up to 600 bar. *Geochim Cosmochim Acta* 2003;67(16):3015–31.
- [37] Ziabakhsh-Ganjii Z, Kooi H. An equation of state for thermodynamic equilibrium of gas mixtures and brines to allow simulation of the effects of impurities in subsurface CO<sub>2</sub> storage. *Int J Greenhouse Gas Control* 2012;11S:21–34.
- [38] Xie Y, Simmons CT, Werner AD. Speed of free convective fingering in porous media. *Water Resour Res* 2011;47(11):W11501. <http://dx.doi.org/10.1029/2011WR010555>.
- [39] Narasimhan TN, Witherspoon PA. An integrated finite difference method for analyzing fluid flow in porous media. *Water Resour Res* 1976;12(1):57–64.
- [40] Noels L, Stainier L, Ponthot JP, Bonini J. Automatic time stepping algorithms for implicit numerical simulations of non-linear dynamics. *Adv Eng Softw* 2002;33(7–10):589–603.
- [41] Nield DA, Bejan A. Convection in porous media. 4th ed. New York Heidelberg Dordrecht London: Springer; 2013.
- [42] Kneafsey TJ, Pruess K. Laboratory flow experiments for visualizing carbon dioxide-induced, density-driven brine convection. *Transport Porous Media* 2010;82:123–39.
- [43] Lindeberg E, Wessel-Berg D. Vertical convection in an aquifer column under a gas cap of CO<sub>2</sub>. *Energy Convers Manage* 1997;38S:229–34.
- [44] Farajzadeh R, Salimi H, Zitha PLJ, Bruining H. Numerical simulation of density-driven natural convection in porous media with application for CO<sub>2</sub> injection projects. *Int J Heat Mass Transfer* 2007;50:5054–64.
- [45] Li H, Yan J. Evaluating cubic equations of state for calculation of vapor–liquid equilibrium of CO<sub>2</sub> and CO<sub>2</sub>-mixtures for CO<sub>2</sub> capture and storage processes. *Appl Energy* 2009;86(6):826–36.
- [46] Li H, Yan J. Impacts of equations of state (EOS) and impurities on the volume calculation of CO<sub>2</sub> mixtures in the applications of CO<sub>2</sub> capture and storage (CCS) processes. *Appl Energy* 2009;86(12):2760–70.
- [47] Bird RB, Stewart WE, Lightfoot EN. Transport phenomena. New York: Wiley; 1960.
- [48] Hassanzadeh H, Pooladi-Darvish M, Keith DW. Scaling behavior of convective mixing with application to geological storage of CO<sub>2</sub>. *AIChE J* 2007;53(5):1121–31.
- [49] Pruess K, Zhang K. Numerical modeling studies of the dissolution-diffusion-convection process during CO<sub>2</sub> storage in saline aquifers. Technical Report LBNL-1243E, Lawrence Berkeley National Laboratory, California, 2008.
- [50] Ghanbari S, Al-Zaabi Y, Pickup GE, Mackay E, Gozalpour F, Todd AC. Simulation of CO<sub>2</sub> storage in saline aquifers. *Chem Eng Res Des* 2006;84:764–75. <http://dx.doi.org/10.1205/cherd06007>.